

# Proton Elastic Scattering and Neutron Distribution of Unstable Nuclei

K.Kaki

Department of Physics, Shizuoka University, Shizuoka 422-8529, Japan

tel:+81-54-238-4744, fax:+81-54-238-0993

e-mail:kkaki@sci.shizuoka.ac.jp

S.Hirenzaki

Department of Physics, Nara Women's University, Nara 630-8506, Japan

## Abstract

We study theoretically how we can determine the neutron density distributions of unstable nuclei from proton elastic scattering. We apply the relativistic impulse model to study the sensitivities of the observables to the density distributions which are expressed in Woods-Saxon form. We find that the both radius and diffuseness of densities can be determined from restricted elastic scattering data in principle. We think this result is helpful to design future experiments.

# 1 Introduction

Since the successful use of the radioactive ion beam, the properties of nuclei far from stability line have been studied extensively in both theoretical and experimental ways [1, 2]. So far clear evidences of neutron skin/halo structure are found for  $^{11}\text{Li}$  [3] and sodium isotopes [4]. There are also many unstable nuclei which are expected to have interesting structures. Thus, to study unstable nuclei is one of the most exciting subjects of nuclear physics.

In experiments, radioactive ions are usually provided as secondary beam and used for nuclear reactions. Since the targets should be heavy enough to use the beam energy efficiently, it is difficult to use electron scatterings as a tool to investigate the nuclear structure. Furthermore, intensities of the secondary beams are much lower than the primary beams used to study the stable nucleus. Because of these facts we think that we need a kind of prescriptions to determine the densities of unstable nucleus from the very restricted experimental data.

So far, to study the structure of the unstable nuclei we have used several kinds of data such as interaction cross sections, neutron-removal cross sections, transverse momentum distributions of projectile fragments, and so on [1, 2]. Using theoretical models of the nuclear reactions, radii of some of unstable nuclei are extracted from the data. Even we can extract the radii of both proton and neutron distributions when we have the information of charge distribution [4, 5]. However, still it seems difficult to determine shapes of density distributions from experimental data.

In this paper, we try to develop a prescription to determine both radius and diffuseness of densities from restricted information of proton elastic scattering. Proton elastic scattering on unstable nuclei has been performed several times [6, 7]. Since theoretical investigations of the data indicate usefulness of the proton elastic scattering [8], it seems very interesting to theoretically study the sensitivities of observables to nuclear structure and to propose which should be observed to determine both radius and diffuseness. We expect that this result is much helpful to design the future experiments.

In section 2, we describe relativistic impulse model which we have used to make a relation

between nuclear density distributions and Dirac optical potentials. We show numerical results and investigate the sensitivities of the observables to nuclear density parameters in section 3. We summarize this paper in section 4.

## 2 Formulation

We calculate Dirac optical potentials using nuclear density distributions based on the relativistic impulse approximation (RIA). Observables of proton elastic scatterings are obtained by solving the Dirac equation with the RIA optical potentials. This model is known to describe the proton-nucleus elastic scattering sufficiently well for wide range of stable-nucleus targets at intermediate energies [9].

The Dirac equation with an RIA optical potential term is given as;

$$\left\{E\gamma^0 - \boldsymbol{\gamma} \cdot \mathbf{p} - M\right\} \psi(\mathbf{p}) = \hat{U}(\mathbf{p}, \mathbf{p}') \psi(\mathbf{p}'), \quad (1)$$

where  $E$  is the energy of proton in center of mass frame,  $M$  is the nucleon mass, and  $\hat{U}(\mathbf{p}, \mathbf{p}')$  is the RIA optical potential which is written as follows;

$$\hat{U}(\mathbf{p}, \mathbf{p}') = \int \frac{d^3k}{(2\pi)^3} \sum_{\alpha} \bar{\psi}_{\alpha}(\mathbf{k} + \frac{1}{2}\mathbf{q}) (-\hat{M}) \psi_{\alpha}(\mathbf{k} - \frac{1}{2}\mathbf{q}). \quad (2)$$

Here,  $\psi_{\alpha}$  indicates the relativistic nucleon wave function in the target,  $\hat{M}$  is Feynman nucleon-nucleon amplitudes, and  $\mathbf{q} = \mathbf{p} - \mathbf{p}'$  is the momentum transfer.

We use the optimal factorization and rewrite the optical potential to so-called 't $\rho$ ' form;

$$\hat{U}(\mathbf{p}', \mathbf{p}) = \frac{1}{4} \text{Tr}_2(-\hat{M}) \hat{\rho}(\mathbf{q}), \quad (3)$$

where the  $\text{Tr}_2$  indicates to take summation of spin of nucleons inside the target. Nuclear density in eq. (3) is written as;

$$\hat{\rho}(\mathbf{q}) = \rho_S(q) + \gamma_2^0 \rho_V(q) - \frac{\boldsymbol{\alpha}_2 \cdot \mathbf{q}}{2M} \rho_T(q). \quad (4)$$

In numerical calculation, we take model densities in coordinate space and calculate each type of  $\rho(\mathbf{q})$  in eq. (4) by Fourier transformation.

The Feynman amplitudes in eqs. (2) and (3) are described as an expansion by complete set of Lorentz covariants as;

$$\hat{M}(p_1, p_2 \rightarrow p'_1, p'_2) = \sum_{\rho_1, \rho_2, \rho'_1, \rho'_2} \Lambda^{\rho'_1}(p'_1) \Lambda^{\rho'_2}(p'_2) \sum_{n=1}^{13} M_n^{\rho_1 \rho_2 \rho'_1 \rho'_2}(p_1, p_2 \rightarrow p'_1, p'_2) \kappa_n \Lambda^{\rho_1}(p_1) \Lambda^{\rho_2}(p_2), \quad (5)$$

where  $\Lambda^\rho(p)$  is the covariant projection operator defined as  $\Lambda^\rho(p) = \frac{1}{2M}(\rho \gamma^\mu p_\mu + M)$ . The  $\rho$  indicates + or - which distinguishes positive- and negative-energy components of the initial and final states. The  $\kappa_n$  is unsymmetrized Fermi covariants shown in Table 1. In the present calculation, we use the IA2 parameterization of the amplitudes in ref. [10].

### 3 Numerical Results

In this section, we show numerical results obtained by the theoretical model described in the last section. First, we have calculated the observables of the proton elastic scattering of  $^{40}\text{Ca}$  at  $T=300\text{MeV}$  and compared them with data in order to check our framework. We calculate the RIA optical potential using the density distribution of relativistic mean field theory (RMFT) [11]. The results are shown in Fig.1. As already discussed [12], we see that the present framework ( the first-order RIA ) gives reasonably good predictions for both differential cross section and analyzing power.

We, then, study the sensitivities of the observables to the shape of neutron density distribution using the model densities. We use Woods-Saxon form defined as;

$$\rho(r) = \frac{\rho_0}{1 + e^{(r-r_0)/a}}, \quad (6)$$

where  $r_0$  is a radius parameter and  $a$  is a diffuseness parameter. As an example, we consider extremely neutron-rich nuclei  $^{60}\text{Ca}$  and calculate the observables. The  $r_0$  parameter is fixed to be 4.48 (fm) which is the half density radius of RMFT result and the  $a$  parameter is varied from 0.5 to 2.0 (fm). We have used the same  $r_0$  and  $a$  parameters for both the scalar and the vector densities appeared in eq. (4). We do not include the tensor density in this model calculation using Woods-Saxon densities since its contribution to the cross section is known to be small. We use the RMFT proton densities here. We show in Table.2 the calculated

root-mean square radius and reaction cross section of each density. The differential cross sections and spin observables are shown in Fig.2.

As shown in Table.2, we find that the reaction cross section is very sensitive to the root-mean-square radius as we expected. The cross section increases monotonically when we increase the diffuseness parameter and namely the root-mean-square radius of the nucleus. We expect to obtain important information on nuclear size by observing reaction cross section. In Fig. 2, we show the angular distribution of observables for each diffuseness value. We can see interesting behavior of the differential cross section. 'The differential cross section has a dip in smaller angles for smaller diffuseness parameters, namely for smaller root-mean-square radii.' We usually think that the dip spacing in the differential cross section can be estimated using a relation  $\Delta q \cdot R \sim \pi$ , where  $\Delta q$  is the difference of momentum transfer corresponding to difference of the scattering angle and R is the nuclear radius. Thus, we expect the first dip angle of the differential cross section will be more forward for larger nucleus. The calculated results shown in Fig. 2 have opposite tendency to this naive expectation, which seems to be useful to determine both radius and diffuseness parameter from data.

In order to clarify the validity of the two observables mentioned above, the reaction cross sections and the first dip angles in the differential cross sections, we calculated the both quantities for various neutron densities for the typical stable nucleus  $^{40}\text{Ca}$ . We have assumed the Woods-Saxon form for neutron densities and varied the parameters in the range of  $3.2 \leq r_0 \leq 4.3$  [fm] and  $0.1 \leq a \leq 0.8$  [fm]. We use the proton density determined by the relativistic mean field theory (RMFT) which has been well established [13].

We show the results in Fig. 3. Each point corresponds to a result calculated with a different neutron density. First, we can see clearly that there exist strong correlation between root-mean-square radius  $r_{rms}$  and reaction cross section  $\sigma_R$  as expected. This correlation is almost independent to the Woods-Saxon density parameters as can be seen in the Fig.3 and thus, is expected to be independent to detail structures of the nucleus. This fact indicates that we can determine  $r_{rms}$  by reaction cross sections in model independent way.

On the other hand, in the same Fig.3, we see that the first dip angles of differential cross sections depend on  $r_{rms}$  in much different way from  $\sigma_R$ . The first dip angle varies in certain range for a fixed  $r_{rms}$ . Thus, in principle, we can determine the shape of the neutron density distribution, both radius and diffuseness, using the two experimental data, reaction cross section and first dip angle of differential cross section. We can fix the  $r_{rms}$  from the reaction cross section and, then, fix the unique combination of the radius and diffuseness parameters by knowing the first dip angle of the differential cross section.

In order to check practical applicability of this idea, we show in Fig. 4 the contour plot of (a) the reaction cross sections and (b) the first dip angles of the differential cross section in the  $r_0$  (radius parameter) -  $a$  (diffuseness parameter) plane of the Woods-Saxon neutron-density distribution. We consider  $^{40}\text{Ca}$  as a typical well-known stable nucleus to check how well we can fix the neutron densities from the reaction cross section and the first dip angle. The proton density determined by RMFT [13] is used in this calculation. We find that the two contour plots show much different behavior and we can find a unique point in the  $r_0$ - $a$  plane using the two kinds of data. In the figure, we show the experimental data point,  $\sigma_R = 51 \text{ [fm}^2\text{]}$  and  $\theta_{dip} = 15.3 \text{ [deg]}$ , by solid circle and experimental uncertainties by hatched area. We have assumed 2 % errors for experimental data. In the actual experiments of proton elastic scattering of unstable nuclei, the experimental errors estimated to be several percent for reaction cross sections and several milliradian for the first dip angles in the case of  $^{56}\text{Ca}$  [14].

We show in Fig.5 neutron densities which are obtained from the reaction cross sections and the first dip angles. For comparison, we also show the RMFT proton and neutron densities in the same figure. We find the neutron density shown by the thick solid line, which reproduce both experimental value, agrees extremely well with the RMFT neutron density around nuclear surface where we expect to find interesting nuclear structure like neutron halo and skin. They agree reasonably well nuclear inside, too. Then, in order to investigate the effects of the errors included in the observations of the reaction cross sections

and the first dip angles, we show the neutron densities determined by the 2 % different values of these observables. Difference of three solid lines indicate the ambiguity of neutron density determination by the present method in the case where we have 2 % error in both data.

We find that we can determine the neutron density distribution only using the reaction cross sections and the first dip angles of proton elastic scattering if they can be measured accurately enough. This is very interesting since we have a possibility to fix both radius and diffuseness parameter by only two experimental numbers which can be measured practically. We do not need to measure very small cross sections at larger angles, which are necessary sometimes to perform standard  $\chi^2$  fit.

As an example of the neutron rich nucleus, we consider  $^{60}\text{Ca}$  and applied the same procedure for  $^{40}\text{Ca}$  explained above. We have used the proton density distribution calculated by RMFT [11] for the  $^{60}\text{Ca}$  target. The reaction cross section and the first dip angles are calculated using the RMFT neutron density first and they are 75.43 [fm<sup>2</sup>] and 12.22 [deg], which are used instead of experimental values. We then replace the neutron densities to the Woods-Saxon form and draw the contour plot as shown in Fig. 6. We assumed the 2 % errors for both the reaction cross sections and the first dip angles, which are shown as hatched area.

In Fig. 7, we compare the obtained neutron densities of the Woods-Saxon form with the RMFT neutron density used to calculate the cross section and the dip angle. We find that their agreement is reasonably well. Although they differ each other about 10 % at  $r < 3$  (fm), they show excellent agreement again around nuclear surface. By comparing the three solid lines, we can also see the ambiguity of neutron density determination in case we have 2 % experimental errors in data of the reaction cross sections and the first dip angles of the differential cross section. This example seems to indicate that our prescription is very useful to determine the neutron density distribution of neutron rich nucleus from restricted data: reaction cross section and the first dip position of differential cross section.

## 4 Summary

We have studied proton elastic scattering theoretically to find a suitable prescription to obtain the nuclear density distributions from restricted experimental data. We think that this prescription must be very useful to study structure of unstable nuclei, for which we can not apply electron scattering.

We have used relativistic impulse model to calculate the observables which are known to describe the elastic scattering well. Sensitivities of observables to density shape are studied with the Woods-Saxon model densities. We have found that the reaction cross section and the first dip position of the differential cross section depend on the neutron density distribution in much different way. We have shown that we can determine both radius and diffuseness parameters in terms of the dip position and reaction cross section. The root-mean-square radius is directly deduced from the reaction cross section, and the whole density shape can be determined by help of the dip position.

In order to demonstrate applicability of the prescription, we have tried to determine the neutron density distribution of  $^{40}\text{Ca}$  and  $^{60}\text{Ca}$  from the reaction cross section and the angle of the first dip of the proton elastic scattering. We find that the density distribution can be determine well if the both data can be observed accurately enough. We think that this prescription is very useful to design future experiments.

In this paper, we focused our attention on the neutron density distribution assuming that the proton densities are known precisely. This assumption is not always correct. In the study of the unstable nuclei, in many cases, the proton density is not known. In such cases, however, we can apply the prescription described in this paper to determine the shape of the matter distribution. This is also valuable since only the root-mean-square radius of the matter has been determined in the previous studies.



## 5 Acknowledgement

We would like to thank Dr. Y.Sugahara for providing a code of extended RMFT and to Prof. H.Toki for valuable discussions. We are also grateful to Prof.R.Seki and Prof. I.Tanihata for their helpful comments. One of us (S.H.) acknowledges many discussions with Prof. K.Kume and Dr. H.Fujita.

Numerical calculations in this paper have been performed using workstations at Information Processing Center of Shizuoka University.

## References

- [1] I.Tanihata, Nucl.Phys. **A520** (1990) 411c; Nucl.Phys. **A522** (1991) 275c; J. Phys. **G22** (1996)157.
- [2] P.G.Hansen, Nucl.Phys. **A533** (1993) 89c; P.G.Hansen, A.S.Jensen, and B.Jonson, Annu.Rev.Nucl.Part.Sci. **45** (1995) 591.
- [3] I.Tanihata et al., Phys. Rev. Lett. **55** (1985)2676.
- [4] T.Suzuki et al., Phys.Rev.Lett. **75** (1995) 3241.
- [5] T.Suzuki et al., Nucl.Phys. **A616** (1997) 286c.
- [6] C.-B.Moon et al., Phys.Lett. **B297** (1992) 39.
- [7] A.A.Korshennikov et al., Phys.Rev. **C53** (1996) R537.
- [8] S.Hirenzaki, H.Toki, and I.Tanihata, Nucl.Phys. **A552** (1993) 57.
- [9] L.Ray, G.W.Hoffmann, and W.R.Coker, Phys.Rep. **212** (1992) 223.
- [10] J.A.Tjon and S.J.Wallace, Phys.Rev. **C35** (1987) 280; Phys.Rev. **C36** (1987) 1085.
- [11] Y.Sugahara and H.Toki, Nucl. Phys. **A579** (1994) 557.
- [12] J.D.Lumpe and L.Ray, Phys.Rev. **C35** (1987) 1040; K.Kaki, Nucl. Phys. **A531** (1991) 478.
- [13] C.J.Horowitz and B.D.Serot, Nucl. Phys. **A368** (1981) 503; C.J.Horowitz, D.P.Murdock and B.D.Serot, Computational Nuclear Physics 1, edited by K.Langanke, J.A.Maruhn and S.E.Koonin ( Springer-Verlag, 1991 ) 129.
- [14] I.Tanihata et al., Phys.Lett. **B287** (1992) 307; I.Tanihata, private communication.
- [15] D.A.Hutcheon et al., Nucl. Phys. **A438** (1988) 429.

Table 1. Definition of  $\kappa_n$  in eq. (5). The momentum  $Q_{ij}$  is defined as  $Q_{ij} = \frac{1}{2m}(p'_i + p_j)$  where  $p$  and  $p'$  correspond to initial and final momentum, respectively.  $\tilde{S}$  is the Fierz exchange operator defined as  $\tilde{S} = \frac{1}{4}(\kappa_1 + \kappa_2 + \kappa_3 + \kappa_4 - \kappa_5)$ .

| $n$ | $\kappa_n$                                | $n$ | $\kappa_n$                    |
|-----|---|-----|-------------------------------|
| 1   | $I$                                       | 6   | $\gamma_2 Q_{11}$             |
| 2   | $\gamma_1 \gamma_2$                       | 7   | $\gamma_1 Q_{22}$             |
| 3   | $\sigma_1 \sigma_2$                       | 8   | $P \gamma_2 Q_{11}$           |
| 4   | $\gamma_1^5 \gamma_2^5 = P$               | 9   | $P \gamma_1 Q_{22}$           |
| 5   | $\gamma_1^5 \gamma_1 \gamma_2^5 \gamma_2$ | 10  | $\gamma_2 Q_{12} \tilde{S}$   |
|     |   | 11  | $\gamma_2 Q_{21} \tilde{S}$   |
|     |   | 12  | $P \gamma_2 Q_{12} \tilde{S}$ |
|     |   | 13  | $P \gamma_1 Q_{21} \tilde{S}$ |

Table 2. Root-mean-square radii and reaction cross sections calculated using the Woods-Saxon neutron densities for  $^{60}\text{Ca}$  case. Results with RMFT density are also shown. We use RMFT proton density [11] and fix the radius parameter of Wood-Saxon neutron densities to  $r_0 = 4.48$  (fm) for all cases shown in this table.

| density | diffuseness         | root-mean-square radius (fm) |        |        |        | reaction cross section<br>(fm <sup>2</sup> ) |
|---------|---------------------|------------------------------|--------|--------|--------|--|
|         | parameter<br>( fm ) | neutron                      |        | proton |        |  |
|         |                     | scalar                       | vector | scalar | vector |  |
| RMFT    | -                   | 4.150                        | 4.133  | 3.555  | 3.550  | 75.34  |
| W-S     | 0.5                 | 3.937                        | 3.937  |        |        | 72.77  |
|         | 1.0                 | 5.083                        | 5.083  |        |        | 87.60  |
|         | 1.5                 | 6.490                        | 6.490  |        |        | 100.9  |
|         | 2.0                 | 7.773                        | 7.773  |        |        | 109.0  |

## Figure Captions

**Figure 1** Observables of proton -  $^{40}\text{Ca}$  elastic scattering at  $T=300\text{MeV}$ . We show (a) differential cross section, (b) analyzing power, and (c) spin-rotation parameter. Solid curves show the calculated results with nuclear density obtained by relativistic mean field theory (RMFT) [11]. Solid circles indicate experimental data taken from ref.[15].

**Figure 2** Observables of proton -  $^{60}\text{Ca}$  elastic scattering at  $300\text{MeV}$  using the Woods-Saxon model densities for neutron distributions. We show (a) differential cross section, (b) analyzing power, and (c) spin rotation parameter. Results with the diffuseness parameter  $a=0.5, 1.0, 1.5, 2.0$  (fm) are shown by solid line, dotted line, dashed line, dash-dotted line, respectively. The RMFT density [11] is used for proton distribution.

**Figure 3** Calculated reaction cross sections (solid triangles) and first dip angles of the differential cross sections (solid circles) are shown as a function of the root mean square radius of neutron distribution for proton- $^{40}\text{Ca}$  elastic scattering at  $T=300\text{ MeV}$ . Proton density distribution determined by RMFT is used [13]. Neutron distribution is assumed to have Woods-Saxon form which parameter is varied in the range of  $3.2 \leq r_0 \leq 4.3$  [fm] and  $0.1 \leq a \leq 0.8$  [fm]. Each point corresponds to the calculated result with different neutron density distribution. For guiding eyes, we connect solid circles calculated with the same diffuseness parameters by solid lines and those with the same radius parameters by dashed lines.

**Figure 4** Contour plots of (a) reaction cross section ( $\text{fm}^2$ ) and (b) first dip position of the differential cross section (degree) in the  $r_0$  (radius parameter)- $a$  (diffuseness parameter) plane of Woods-Saxon neutron densities for  $^{40}\text{Ca}$  at  $T=300\text{ MeV}$ . We use RMFT distribution [13] for the proton density. Experimental values are shown by dotted lines in both plots, which cross at the point indicated by the solid circle. Experimental error is assumed to be 2 % and shown as the hatched area in (a).

**Figure 5** Neutron density distributions of  $^{40}\text{Ca}$  determined from the reaction cross sections and first dip angles are shown by solid lines. Thick solid line corresponds to the density which reproduce the both experimental values shown as a solid circle in Fig.4. Solid lines with a and c show the densities correspond to points a and c in Fig.4 (a) . For comparison, the RMFT neutron and proton density distributions are shown by dotted and dash-dotted line, respectively.

**Figure 6** Contour plots of (a) reaction cross section ( $\text{fm}^2$ ) and (b) first dip position of the differential cross section (degree) in the  $r_0$  (radius parameter)- $a$  (diffuseness parameter) plane of Woods-Saxon neutron densities for  $^{60}\text{Ca}$  at  $T=300$  MeV. We use RMFT distribution [11] for the proton density. Dotted lines indicate the calculated values with RMFT neutron density, which cross at the point indicated by the black solid circle. The hatched area in (a) indicates 2 % errors for the values with RMFT neutron density.

**Figure 7** Neutron density distributions of  $^{60}\text{Ca}$  determined from the reaction cross sections and first dip angles are shown by solid lines. Thick solid line corresponds to the density which reproduce the both values obtained with the RMFT neutron density shown as a solid circle in Fig.6. Solid lines with a and c show the densities correspond to points a and c in Fig.6 (a) . For comparison, the RMFT neutron and proton density distributions are shown by dotted and dash-dotted line, respectively.

Figure 1

Figure 2



Figure 3

Figure 4 (a)

Figure 4 (b)

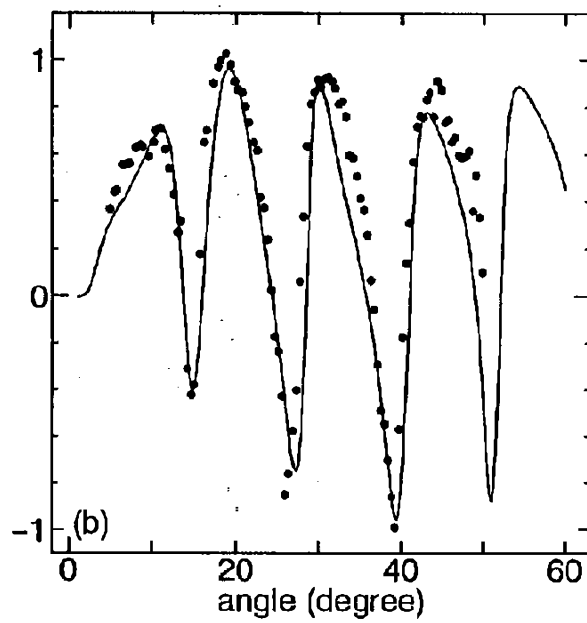
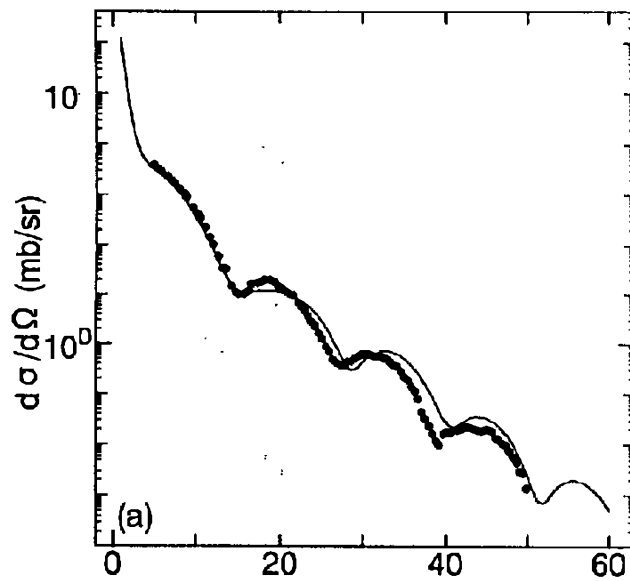
Figure 5

Figure 6 (a)

Figure 6 (b)

Figure 7

Figure 1



40Ca at 300 MeV

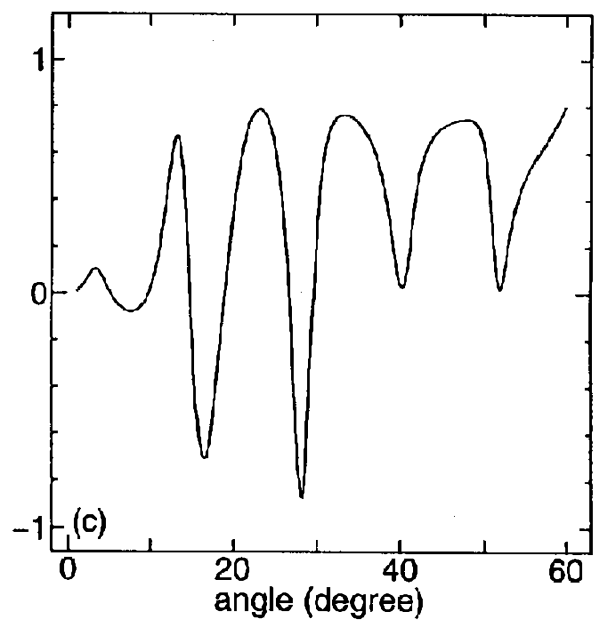
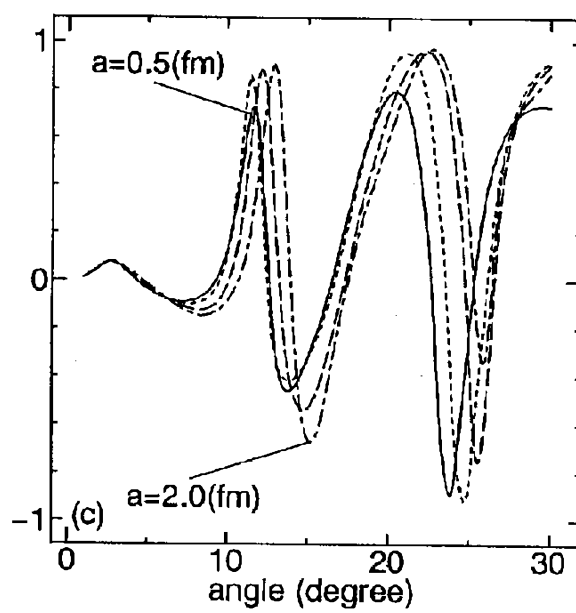
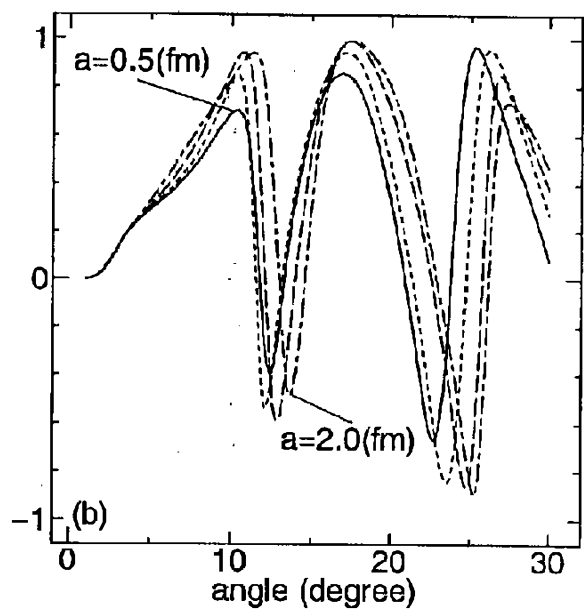
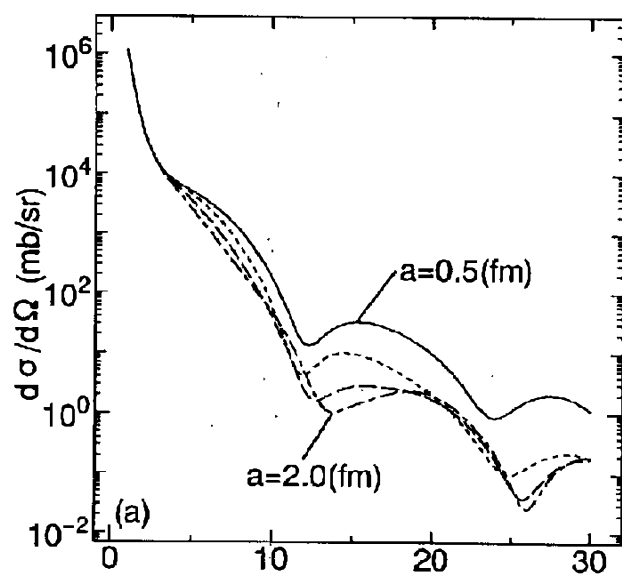




Figure 2



60Ca at 300 MeV

Figure 3

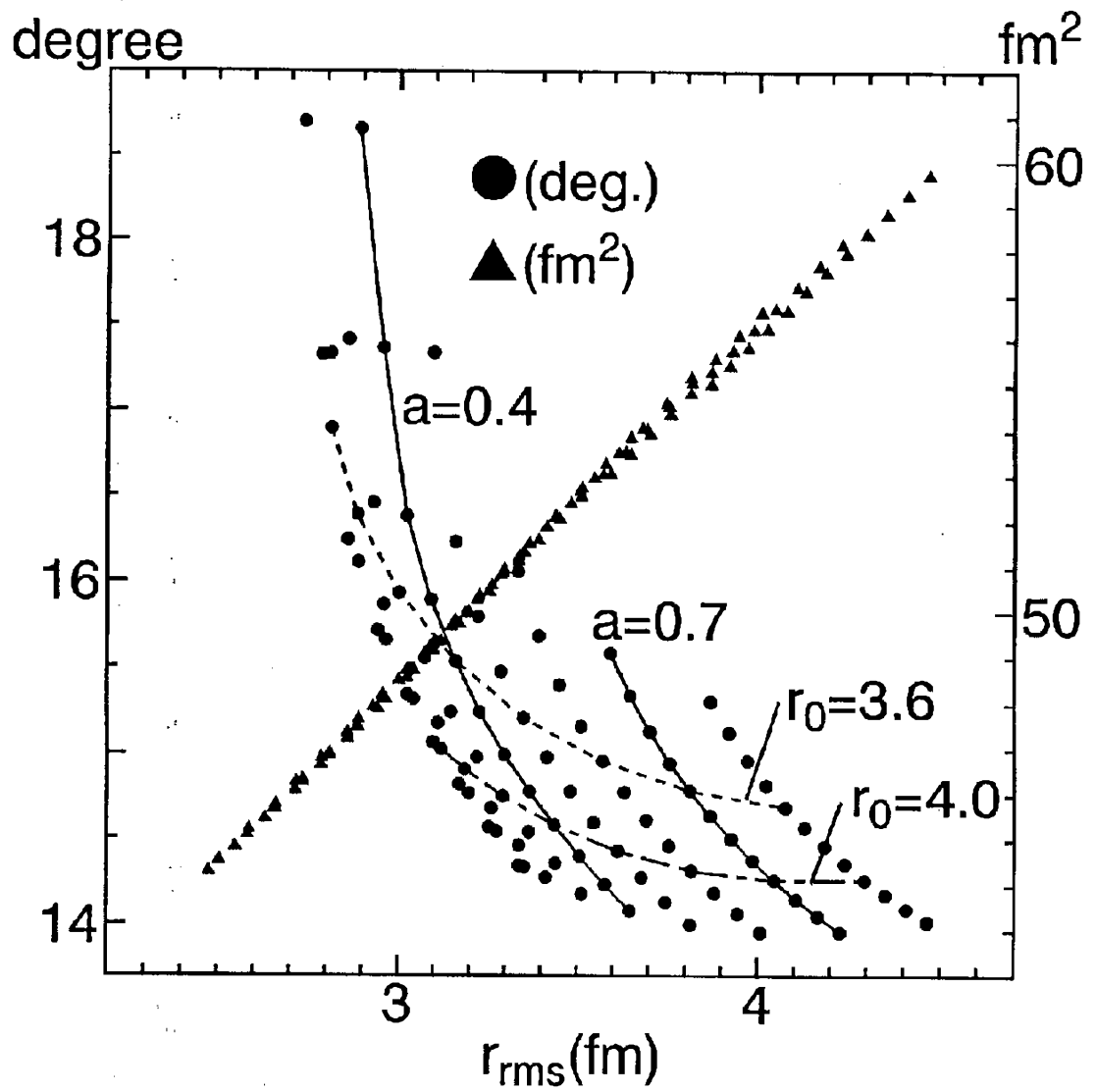


Figure 4 (a)

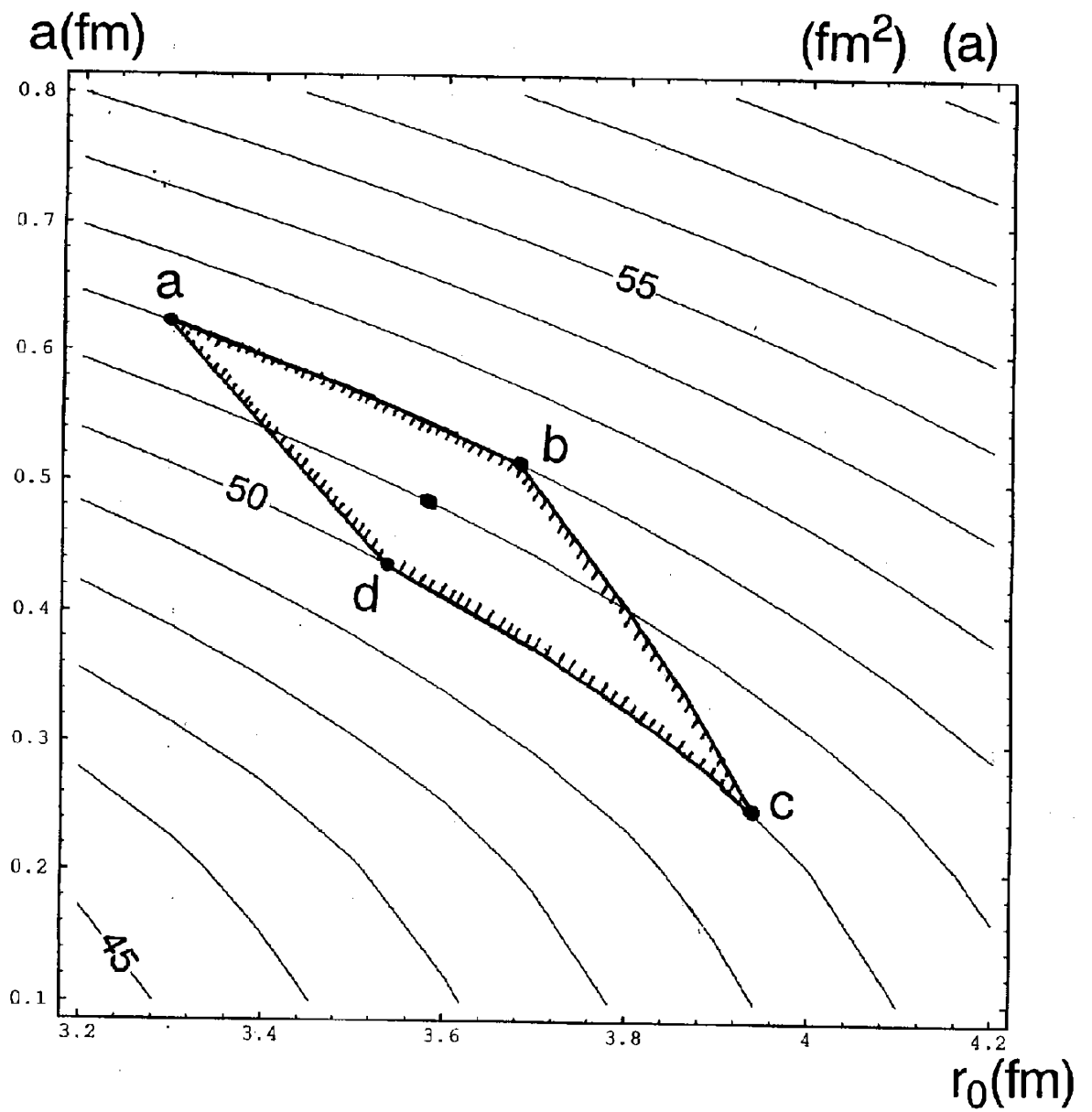


Figure 4 (b)

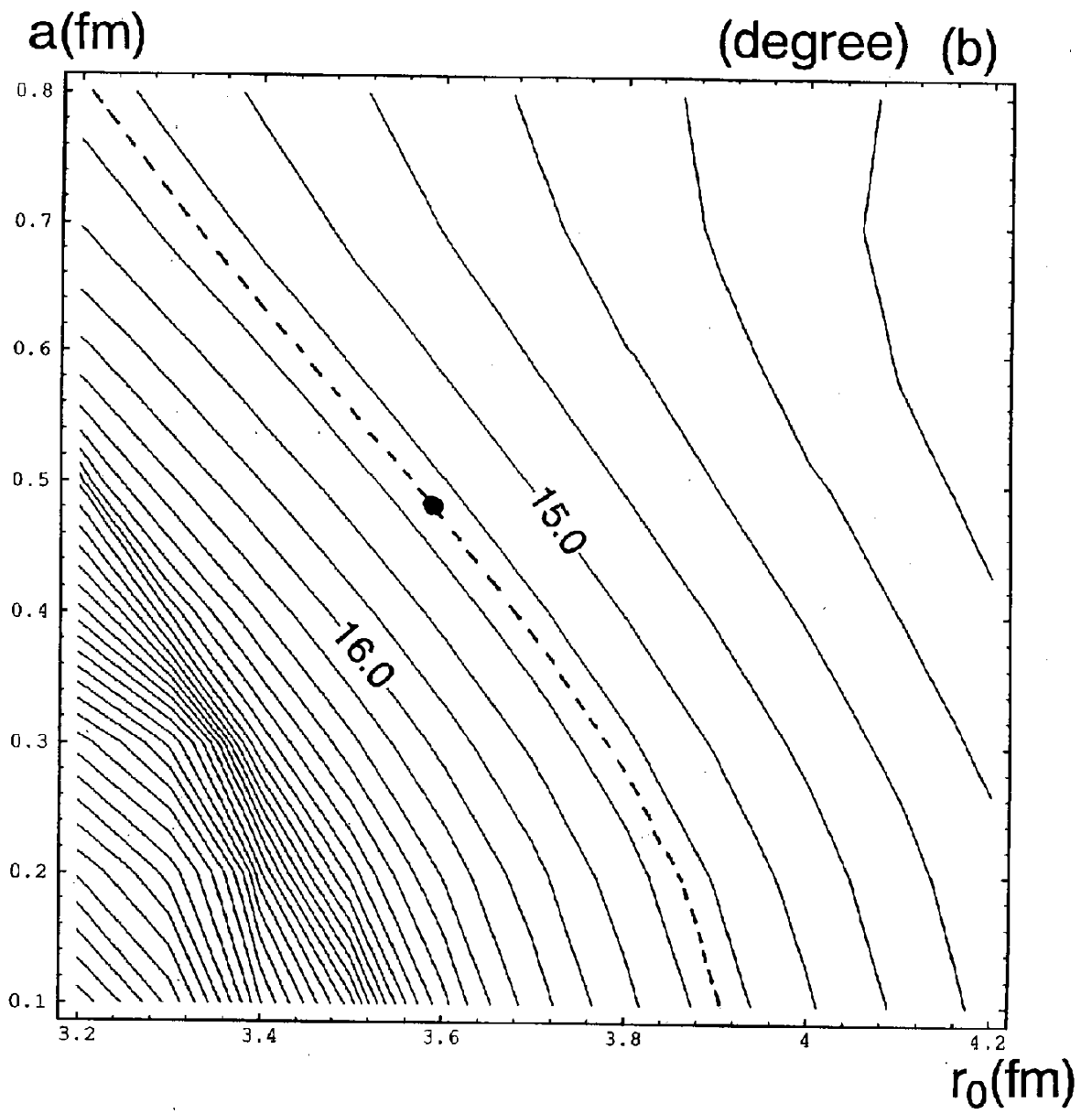


Figure 5

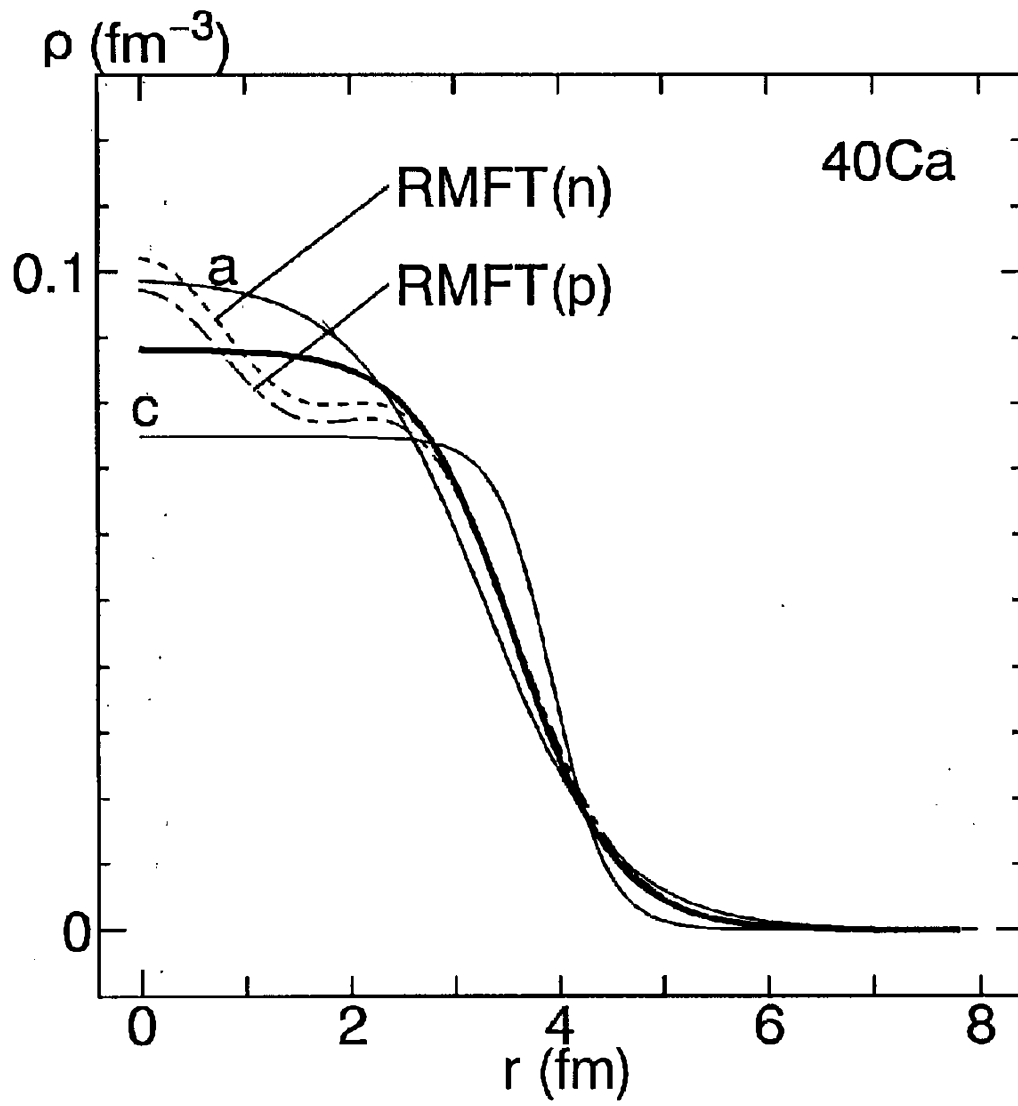


Figure 6 (a)

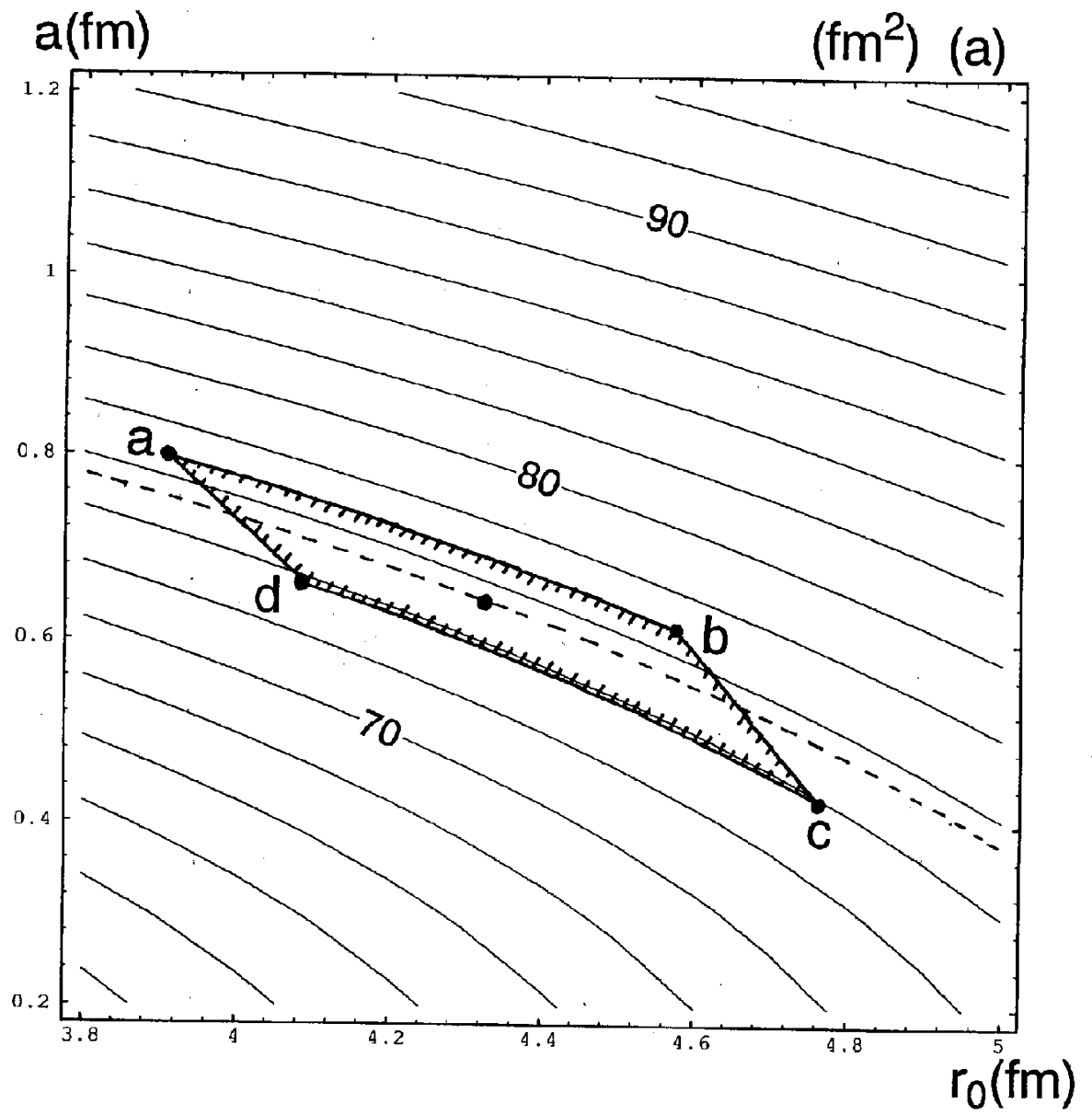


Figure 6 (b)

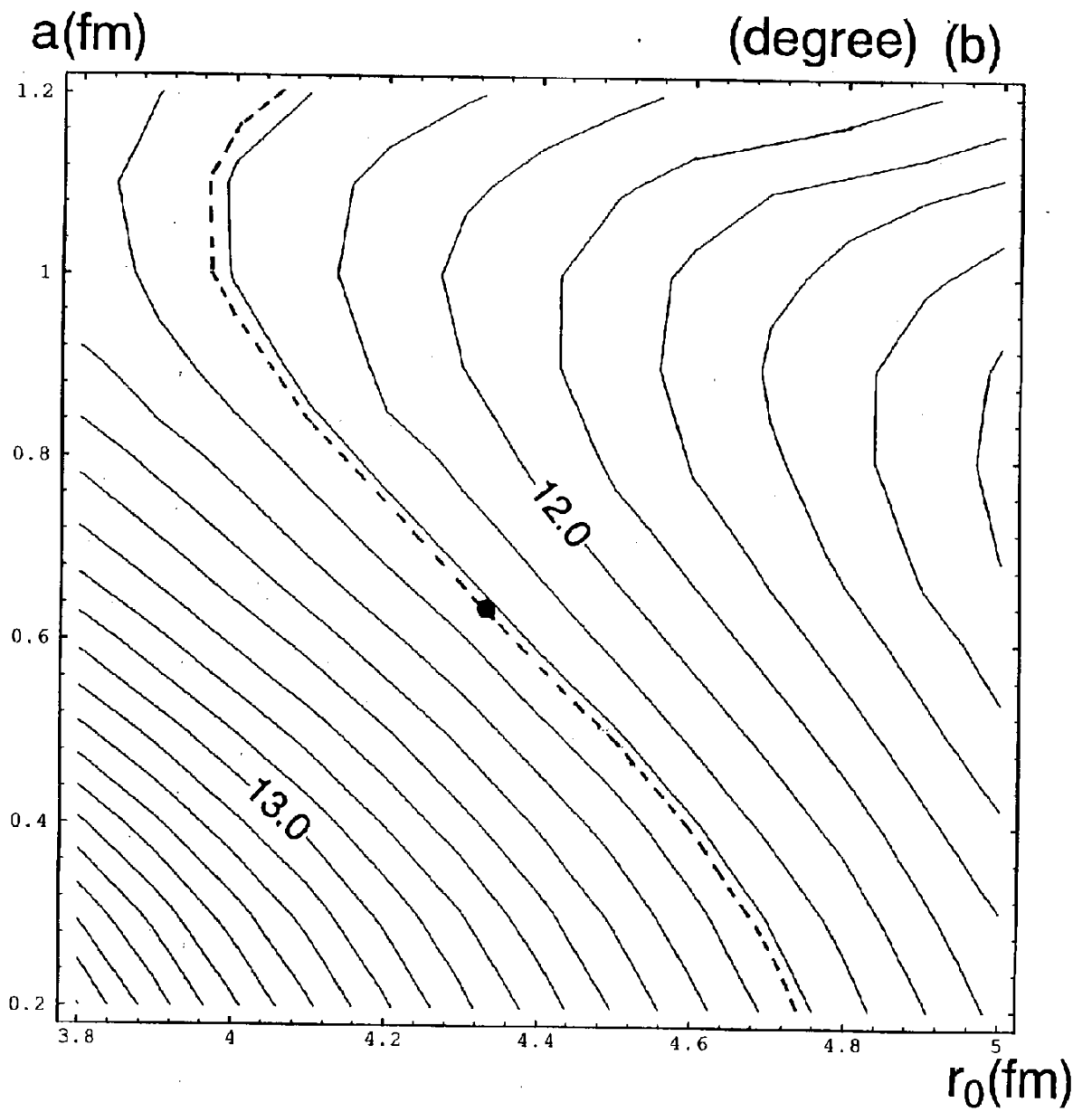


Figure 7

